PHYSICAL REVIEW MATERIALS **3**, 064803 (2019)

Editors' Suggestion

Molecular beam epitaxy of electron-doped infinite-layer $Ca_{1-x}R_xCuO_2$ thin films

Ai Ikeda, Yoshiharu Krockenberger, and Hideki Yamamoto
NTT Basic Research Laboratories, NTT Corporation, 3-1 Morinosato-Wakamiya, Atsugi, Kanagawa 243-0198, Japan

(Received 4 March 2019; published 17 June 2019)

Thin films of the electron-doped infinite-layer $Ca_{1-x}R_xCuO_2$, with $R = La^{3+}$, Nd^{3+}, and Ce^{4+}, have been synthesized using molecular beam epitaxy. The solubility limits of R in $Ca_{1-x}R_xCuO_2$ are 0.060 ± 0.002, 0.080 ± 0.010, and <0.01 for $R = Nd^{3+}$, La^{3+}, and Ce^{4+}, respectively. Using high-resolution reciprocal space mapping we show that the in-plane lattice constants of $Ca_{1-x}R_xCuO_2$ follow the same trend as is observed for other cuprates with square-planar coordinated copper, i.e., elongation of the Cu-O bond length upon electron doping. We measured the temperature dependencies of the resistivity and the Hall coefficient to trace the influence of the doped charge carriers on the electronic response. We show that the Hall coefficient is negative below 300 K and that the R substitution level is insufficient to achieve a positive Hall coefficient, a necessary prerequisite for superconductivity.

DOI: 10.1103/PhysRevMaterials.3.064803

I. INTRODUCTION

Superconductivity in cuprate superconductors is linked to the copper-oxygen planes and this is the common element among all cuprate superconductors. While generally the detailed crystallographic arrangement of these cuprates is complex, the infinite-layer phase is the simplest arrangement of a cuprate [Fig. 1(a)]. In there, an alkaline-earth element separates the CuO_2 planes [1] and it is this simplicity that draws significant attention. Cuprates with the infinite-layer structure are, however, thermodynamically unstable and high-pressure synthesis methods are necessary to synthesize them in a bulk form [2]. Such high-pressure synthesis methods impose a significant limitation on what kind of measurement techniques can be applied on the sample and this is particularly true for powder materials as the growth of single crystals remains elusive. While the infinite-layer phase $CaCuO_2$ has been known for long, high-temperature superconductivity was assumed to be immanent of this phase [3]. Certainly, infinite-layer $CaCuO_2$ may not just be an independent cuprate phase worthwhile being studied, but an indispensable ingredient of high-temperature cuprate superconductors that contain more than two CuO_2 planes in a unit block, e.g., $Bi_2Sr_2Ca_2Cu_3O_{10+\delta}$ [4]. Such multilayer cuprates are well known for their exceptional high superconducting transition temperatures. In particular, for the growth of $Bi_2Sr_2Ca_2Cu_3O_{10+\delta}$ ($T_c = 110$ K), high oxygen pressures are not required [5], an important prerequisite for the growth of single crystals.

Using molecular beam epitaxy, however, the infinite-layer phase can be stabilized in single-crystalline form [6–11], a mandatory first step for further investigations into the electronic response [8]. In our earlier paper, we have shown that single-crystalline infinite-layer $CaCuO_2$ is an insulator [9]. The subtleties of the microscopic defects hampering the electron transport are not easy to be quantified even with electron microscopy methods and more needs to be done to gauge them. Nonetheless, tuning this insulating state toward a metal has been subject of several reports targeting the growth of hole-doped $CaCuO_2$ materials [12–15], where the divalent calcium is replaced by a monovalent alkaline-earth metal element, i.e., Na or Li. Electron doping, however, remains still elusive for $CaCuO_2$ and this is particularly true for high-quality single-crystalline materials [16,17].

In this paper, we report the growth of electron-doped infinite-layer $Ca_{1-x}R_xCuO_2$ ($R = La^{3+}$, Nd^{3+}, and Ce^{4+}) thin films by reactive molecular beam epitaxy to trace their electronic response. To ensure the crystal quality of these thin films, we conducted scanning transmission electron microscopy combined with atomically resolved electron energy loss spectroscopy. In combination with electrical transport measurements, we conclude that defects-driven electronic structure modification that still remains after the R substitution up to the solubility limits inhibits the superconducting transition.

II. EXPERIMENTAL DETAILS

Ultra-high-quality infinite-layer $Ca_{1-x}R_xCuO_2$ ($R = La^{3+}$, Nd^{3+}, and Ce^{4+}) thin films were grown on (001) $(LaAlO_3)_{0.3}(SrAl_{0.5}Ta_{0.5}O_3)_{0.7}$ (LSAT) substrates in a custom designed molecular beam epitaxy system with 10 elemental sources. Ca, Cu, La, Nd, and Ce were coevaporated by electron guns. The atomic beam fluxes of Ca, Cu, La, and Nd were controlled by electron impact emission spectroscopy (EIES) [18]. For the Ce flux control, a quartz crystal microbalance was used [19]. The typical growth rates and times are approximately 1 Å/s and 10 min, respectively. During the growth, the surface structure of the thin film was monitored *in situ* by reflection high-energy electron diffraction. A steady and strong oxidizing environment was provided by a custom designed atomic oxygen source operated at 13.56 MHz [radio frequency (rf)]. We carefully optimized the oxidizing conditions as well as the substrate temperature (T_s) for different R and x. We varied the rf power of the atomic oxygen source as well as oxygen flow rate in the

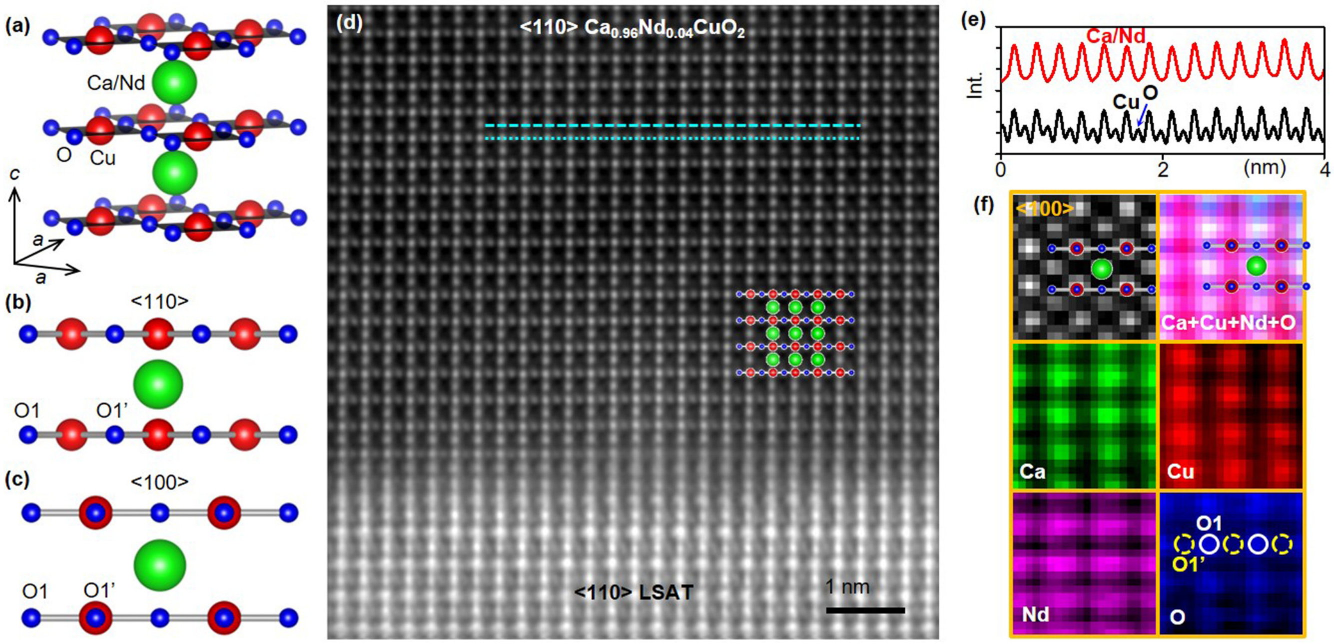

FIG. 1. (a) Crystal structure of infinite-layer $Ca_{1-x}Nd_xCuO_2$. (b), (c) Infinite-layer structure in the [110] and [100] projections, respectively. In the [110] projection, the stacking sequence along the in-plane direction at each atomic site is homologous. In the case of the [100] projection, 50% O [denoted as O1′ in (c)] and Cu are located at same atomic position, while the other 50% O [denoted as O1 in (c)] are independent. (d) Cross-sectional inverted ABF-STEM image of the interface of infinite-layer $Ca_{0.96}Nd_{0.04}CuO_2$ thin film grown on (001)LSAT substate taken along the [110] direction. (e) The intensity profiles of the inverted ABF image taken along the dashed (Ca/Nd layer) and dotted (CuO_2 layer) lines in (d). (f) HAADF-STEM image of $Ca_{0.96}Nd_{0.04}CuO_2$ thin film along [100] direction and EELS elemental maps of Ca *L*, Cu *L*, Nd *M*, and O *K* edges.

range of 200 to 400 W and 0.5 to 3.0 sccm, respectively. T_s was measured by a radiation pyrometer (Japan Sensor) and varied from 550 °C to 620 °C. Optimal oxidizing conditions are at 300 W with an oxygen flow of 0.8–2.5 sccm corresponding to an oxygen background pressure of $\sim 10^{-6}$ Torr while optimal T_s is 590 °C. After the growth, films were rapidly cooled under ultrahigh vacuum conditions (10^{-9} Torr).

While the stoichiometry of the infinite-layer films is controlled by the EIES, an independent verification using inductively coupled plasma (ICP) analysis allows to narrow the error bars on the stoichiometry close to ± 0.002 (± 0.2 %) on x. The structural characterizations were done by high-resolution x-ray diffraction (XRD) measurements with monochromatic Cu $K\alpha_1$ radiation on a Bruker D8 4-circle diffractometer. High-resolution scanning transmission electron microscopy (STEM) measurements were performed on an aberration-corrected 200-keV JEOL ARM-200F microscope equipped with an electron energy loss spectrometer (Gatan). Specimens for the cross-sectional STEM measurements were prepared using focused ion beam milling. Annular bright field (ABF) and high-angle annular dark field (HAADF) images were collected with a rate of 0.5–1.0 s/image, and integrated to minimize image shifts during acquisition [20,21]. Atomically resolved electron energy loss spectroscopy (EELS) elemental maps of infinite-layer $Ca_{1-x}Nd_xCuO_2$ thin films using the Ca $L_{2,3}$ (350 eV), Cu $L_{2,3}$ (931 eV), Nd $M_{4,5}$ (978 eV), and O K edges (532 eV) were simultaneously taken with the corresponding HAADF-STEM image.

Electrical transport measurements were done in a Quantum Design Dynacool physical property measurement system. We measured temperature dependencies of resistivity (ρ) between 300 to 2 K using a standard four-probe method with silver electrodes. Low-temperature ρ-T measurements with a dilution refrigerator were performed under magnetic fields ($\mu_0 H$) applied perpendicular to the CuO_2 plane of the films. A standard six-probe Hall bar with an aspect ratio of 0.25 of voltage and current channel width was patterned into the films using photolithography and ion milling techniques. Measurements of the Hall coefficient (R_H) were performed in the temperature range between 300 to 2 K. For all Hall coefficient measurements we measured the Hall resistance (R_{xy}) over the magnetic field ±14 T[1] at constant temperature and observed that the $\mu_0 H$ dependence of R_{xy} is linear for all measurements. The R_H values were determined from the slope of the linearly fitted lines.

Through the structural characterization, we found the solubility limits of R ions to be 0.08, 0.06, and <0.01 for La^{3+}, Nd^{3+}, and Ce^{4+} ions, respectively. Hereafter, we will present structural as well as electronic transport properties for $Ca_{1-x}R_xCuO_2$ thin films with x below their solubility limits.

III. RESULTS AND DISCUSSION

ABF imaging is a powerful technique to visualize light elements like oxygen (atomic number Z = 8). We performed ABF-STEM on infinite-layer $Ca_{0.96}Nd_{0.04}CuO_2$ thin films to

---

[1] For $CaCuO_2$, R_H was recorded between ±2 T.

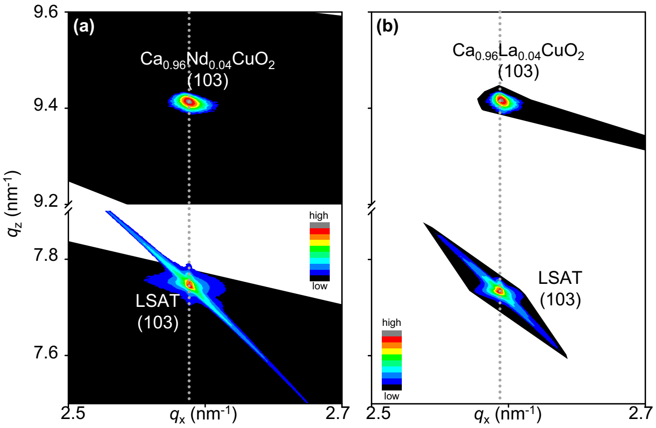

FIG. 2. High-resolution reciprocal space maps of inifinite-layer $Ca_{0.96}Nd_{0.04}CuO_2$ (a) and $Ca_{0.96}La_{0.04}CuO_2$ (b) thin films grown on (001)LSAT substrates.

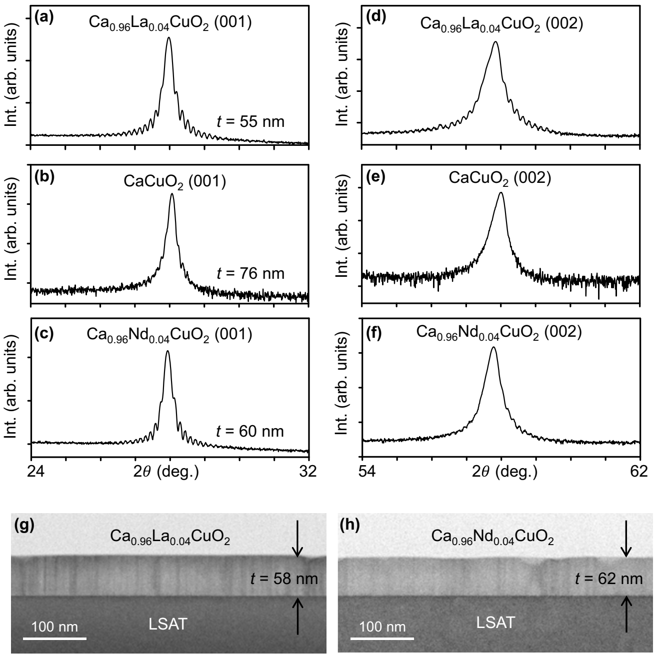

FIG. 3. High-resolution XRD patterns around the (001) and (002) reflections of infinite-layer $Ca_{0.96}La_{0.04}CuO_2$ (a), (d), $CaCuO_2$ (b), (e), and $Ca_{0.96}Nd_{0.04}CuO_2$ (c), (f) thin films grown on (001)LSAT substrates. Cross-sectional transmission electron microscopy (TEM) images of $Ca_{0.96}La_{0.04}CuO_2$ (g) and $Ca_{0.96}Nd_{0.04}CuO_2$ (h) thin films grown on (001)LSAT substrates. The film thicknesses (t) calculated from the Laue fringes in XRD peaks are 55, 76, and 60 nm for $Ca_{0.96}La_{0.04}CuO_2$, $CaCuO_2$, and $Ca_{0.96}Nd_{0.04}CuO_2$ thin films, respectively, which agrees well with t estimated from the TEM images [$t = 58$, 70, and 62 nm for $Ca_{0.96}La_{0.04}CuO_2$, $CaCuO_2$ (not shown), and $Ca_{0.96}Nd_{0.04}CuO_2$ thin films, respectively].

confirm their atomic arrangements. Along the [110] projection [see Fig. 1(b)], oxygen atoms are located between Cu atoms, and therefore visible without overlap with other heavy elements. Figure 1(d) shows a contrast-inverted (atomic positions appear bright) cross-sectional ABF-STEM image of the film taken along the [110] direction. Observed atomic columns correspond to Ca/Nd, Cu, and O atoms of infinite-layer structure. The intensity profiles of the inverted ABF image along Ca/Nd and CuO_2 layers do not show any additional peaks that may result from possible impurity phases or defects [Fig. 1(e)]. Apparently, in $Ca_{1-x}Nd_xCuO_2$, the Ca/Nd sites are not ordered and this is related to the equal heights of the electron counts. In general, the atomic number sensitivity for ABF detectors is inferior (approximately proportional to $Z^{1/3}$) to that of HAADF detectors (approximately proportional to $Z^{1.4}$). To distinguish between the different elements in the infinite-layer cuprates, we analyzed the corresponding HAADF maps by EELS for the Ca $L_{2,3}$, Cu $L_{2,3}$, Nd $M_{4,5}$, and O K edges, and combined them with HAADF-STEM images. Elementally resolved columns observed in Fig. 1(f) describe the atomic arrangement of the infinite-layer structure. The atomic columns for the Nd M edge are aligned at an equal distance. Therefore, it is evident that Nd^{3+} ions randomly occupy the Ca sites.

In the O K EELS map [Fig. 1(f)], the intensities of the positions marked by dashed circles (O1′) are significantly weaker than those marked by solid ones (O1), although the occupancy of both sites is formally equivalent. As is detected, the intensity of the O K edge is influenced by the presence of heavy atoms (Cu) along the [100] direction [see Fig. 1(c)]. Such intensity modulations are expected and commonly observed [22,23].

By substituting Nd^{3+} ions for Ca^{2+} ions, the lattice parameters are expected to vary from those of $CaCuO_2$ because of the difference in ionic sizes. The in-plane (a) and out-of-plane (c) lattice parameters determined from the STEM intensity profile are 3.858 ± 0.010 Å and 3.232 ± 0.050 Å for $Ca_{0.96}Nd_{0.04}CuO_2$ thin films. Those values agree with a- and c-axis lengths determined from XRD reciprocal space map (RSM) of the corresponding thin film [Fig. 2(a)] ($a = 3.862$ Å and $c = 3.168$ Å). The a-axis length of infinite-layer $Ca_{0.96}Nd_{0.04}CuO_2$ thin film is elongated compared to $CaCuO_2$ ($a = 3.853$ Å[24]). The ionic radius of Nd^{3+}(1.11 Å for the coordination number of 8) is smaller than that of Ca^{2+}(1.12 Å) [25], and therefore the expansion in a-axis length by Nd^{3+} substitution cannot be assigned to the size effect. Instead, the Cu-O bond length expands as the doped electrons occupy the antibonding $Cu3d_{x^2-y^2}$-$O2p_{x,y}$ orbitals as observed for other electron-doped cuprate systems [26]. This is further verified by the fact that the a-axis length monotonically increases with increasing Nd^{3+} concentration and the trend of a-axis length expansion holds also for La^{3+} substitution. Note that the effect of epitaxial strain on the change in the lattice parameters is negligible because $Ca_{1-x}R_xCuO_2$ films are partially relaxed on LSAT substrates.

As far as the c-axis spacing is concerned, the ionic size effect is dominant. While the c-axis length shrinks upon Nd^{3+} substitution, it expands for La^{3+} substitution. In general, such structural distortions, as observed here, are expected to create defects, such as dislocation, as they tend to destabilize the equilibrium conditions of the crystal. However, this is not true for the infinite-layer $CaCuO_2$ system. Figures 3(a)–3(f) show $2\theta/\theta$ scans of infinite-layer $Ca_{0.96}La_{0.04}CuO_2$, $CaCuO_2$, and $Ca_{0.96}Nd_{0.04}CuO_2$ thin films. Using the full width at half-maximum criteria for the peaks around the (001) reflection

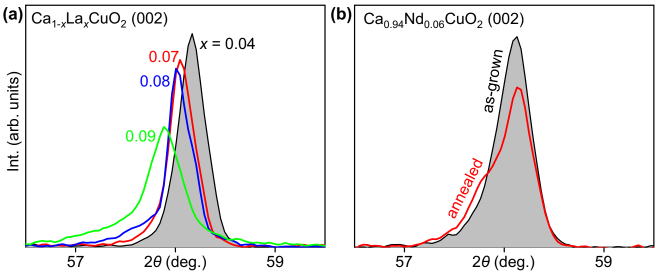

FIG. 4. $2\theta/\theta$-scanned x-ray diffraction patterns around the (002) reflections of infinite-layer $Ca_{1-x}La_xCuO_2$ ($x = 0.04$, 0.07, 0.08, and 0.09) (a) and $Ca_{0.94}Nd_{0.06}CuO_2$ (b). In (b) spectra for the as-grown and annealed films are shown. The latter was annealed with atomic oxygen (rf power of 300 W and oxygen flow rate of 0.8 sccm) at 280 °C for 10 min.

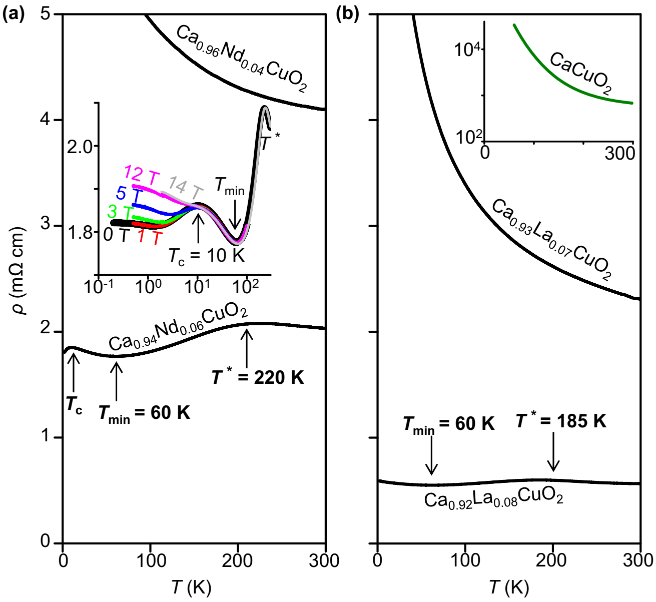

FIG. 5. Temperature dependencies of resistivity for infinite-layer $Ca_{1-x}Nd_xCuO_2$ ($x = 0.04$, 0.06) (a) and $Ca_{1-x}La_xCuO_2$ ($x = 0.07$, 0.08) (b) thin films grown on (001)LSAT substrates. The inset in (a) shows enlarged view of ρ-T curves of $Ca_{0.94}Nd_{0.06}CuO_2$ thin film down to 200 mK under magnetic field of 0, 1, 3, 5, 12, and 14 T applied perpendicular to the ab planes. For comparison, the ρ-T curve for $CaCuO_2$ is shown in the inset in (b). T^* and T_{min} are defined as onset temperatures for the pseudogap and resistivity minimum, respectively. T_c is superconducting critical temperature. The current density used is 30 A/cm^2, which is far below the superconducting critical current density of infinite-layer cuprates where $J_c = 5.9$ MA/cm^2 [56].

of $Ca_{0.96}R_{0.04}CuO_2$ and $CaCuO_2$ thin films [Figs. 3(a)–3(c)], the La^{3+} or Nd^{3+} substituted films have an enhanced coherent crystal volume. This is further evidenced by clear Laue oscillations observed for $Ca_{0.96}R_{0.04}CuO_2$ films in contrast to $CaCuO_2$ film. We determined the coherent crystalline volume of the infinite-layer films from Laue oscillations observed here, and found that its thicknesses ($t = 55$ and 60 nm for $R =$ La and Nd, respectively) [27] well agree with the t estimated from cross-sectional TEM images ($t = 58$ and 62 nm for $R =$ La and Nd, respectively) for the corresponding films [Figs. 3(g) and 3(h)].

On the other hand, the (002) peaks show asymmetric peak broadening toward smaller 2θ values irrespective of the doping value between $x = 0$–0.04 [Figs. 3(d)–3(f)]. As shown in Fig. 4(a), the peak broadening is more pronounced when x exceeds 0.08 while the peak intensities are significantly reduced. The asymmetric Bragg peak broadening is commonly due to anisotropic atomic displacements causing one-dimensional lattice distortions [28,29]. Such one-dimensional confined defects have been reported for overdoped infinite-layer $Sr_{1-x}La_xCuO_2$ thin films, where an intergrown secondary phase $Sr_{1-x}La_xCuO_2$ with the $2\sqrt{2}a \times 2\sqrt{2}a \times c$ modulated superstructure, the so-called "long-c" phase forms a striped defect structure [30], and this is linked to the absence of superconductivity in overdoped $Sr_{1-x}La_xCuO_2$. The observed peak splitting for $x \geqslant 0.08$ may be associated to the appearance of the "long-c" phase in $Ca_{1-x}R_xCuO_2$ system, although the uncertainty (Δ) of c-axis length when estimated from the (002) peak broadening is much smaller ($\Delta = \pm 0.005$ Å) compared to what has been seen in the "long-c" phase $Sr_{1-x}La_xCuO_2$, where the elongation of c-axis length is $\Delta = 0.2$ Å [6,31–33]. For comparison, we tried to convert the infinite-layer $Ca_{1-x}Nd_xCuO_2$ into a "long-c" phase $Ca_{1-x}Nd_xCuO_2$ by placing the infinite-layer cuprate films under strongly oxidizing conditions [Fig. 4(b)]. To some extent, the "long-c" phase $Ca_{1-x}Nd_xCuO_2$ was formed and this process is quite similar to what is known in the $Sr_{1-x}R_xCuO_2$ system [34]. The infinite-layer phase persists up to $x = 0.06$ and 0.08 for Nd^{3+} and La^{3+}, respectively, and we defined these thresholds as the corresponding solubility limits. Any further increase in x above the solubility limit is accompanied by the appearance of an impurity phase, the two-leg ladder compound $Ca_{14-x}R_xCu_{24}O_{41}$ [35–38]. There might be, however, other unspecified phases [9], whose volumes are below the resolution limit of x-ray diffraction.

In complex transition metal oxides, defects are omnipresent and this is particularly true for cuprates. Those defects tend to accumulate preferably above and below the CuO_2 planes, where other oxides damp their influences on the CuO_2 planes. In infinite-layer cuprates, the CuO_2 planes are simply sandwiched by Ca^{2+}/R^{3+} having no flexibility to accommodate charge imbalances originating from defects in the CuO_2 planes and any disorder may result in immediate termination of T_c. The electron conduction is highly sensitive to such defects which we cannot quantify by x-ray scattering. Figure 5 shows the temperature dependencies of resistivity for different x values. $Ca_{0.96}Nd_{0.04}CuO_2$ and $Ca_{0.93}La_{0.07}CuO_2$ thin films have an insulating character ($d\rho/dT < 0$) below 300 K. Larger x values result in lower resistivity values and if $x = 0.06$ for $R =$ Nd the resistivity is three orders of magnitude lower than when compared to $x = 0.00$ [9,39,40]. A similar trend is seen for $R =$ La. Even though the absolute resistivity value is now significantly lower, the electronic conduction is far from a two-dimensional Fermi liquid. Instead, the ρ-T curves for $Ca_{0.94}Nd_{0.06}CuO_2$ and $Ca_{0.92}La_{0.08}CuO_2$ show upturns around 60 K. For $Ca_{0.94}Nd_{0.06}CuO_2$, the resistivity shows an unusual drop below 10 K. More importantly, however, is the magnetic field dependency of this abrupt resistivity drop as highlighted in the inset in Fig. 5(a). This

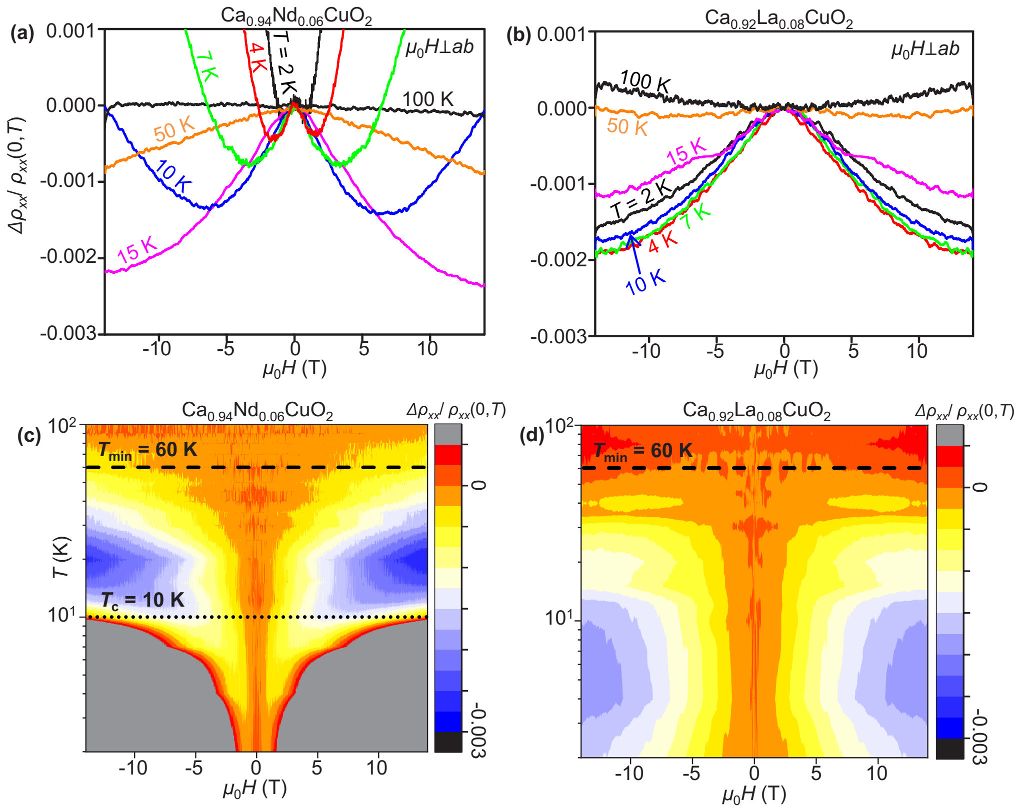

FIG. 6. Magnetoresistance $\Delta\rho_{xx}/\rho_{xx}(0,T)$ of $Ca_{0.94}Nd_{0.06}CuO_2$ (a) and $Ca_{0.92}La_{0.08}CuO_2$ (b) thin films grown on LSAT substrates, where $\Delta\rho_{xx} = \rho_{xx}(\mu_0 H, T) - \rho_{xx}(0,T)$. The temperature ranges below 100 K. Magnetic field is applied perpendicular to the *ab* planes. Linear interpolated contour plot of $\Delta\rho_{xx}/\rho_{xx}(0,T)$ as a function of magnetic field ($-14\ \text{T} \leqslant \mu_0 H \leqslant 14$ T) and temperature ($T = 2$, 4, 7, 10, 12, 15, 20, 25, 30, 35, 40, 45, 50, 60, 70, 80, 90, and 100 K) for corresponding $Ca_{0.94}Nd_{0.06}CuO_2$ (c) and $Ca_{0.92}La_{0.08}CuO_2$ (d) films.

magnetic field dependence of resistivity suggests that some fraction of the film may have undergone a superconducting transition and similar phase transitions have been reported for pnictides [41].

At higher temperatures, a humplike structure around 200 K can be identified. Microscopic phase separation phenomena [42] have been suspected to be responsible for the observed temperature trend. On the other hand, it is throughout possible to associate the observed hump to a electronic ordering phenomena, e.g., charge ordering. Particularly, the electron-doped telephone number compound $La_{6-y}Sr_yCa_8Cu_{24}O_{41}$ does have a pronounced charge ordering phenomena between 800 ($y = 0$) and 100 K ($y = 6$) [35], and this charge order may be present in the infinite-layer system as well. One would expect that a finite influence of the magnetic field on the charge ordering phenomena does take place and consequently enhances the absolute resistivity. Nonetheless, this is not observed in $Ca_{1-x}R_xCuO_2$. Instead of the charge ordering scenario, the hump of resistivity can be linked to the formation of the pseudogap in the electronic density of states, as generally seen in cuprate superconductors. The observed tendency that the humplike feature shifts toward lower temperatures with increasing x suggests the evolution of a pseudogap in infinite-layer $Ca_{1-x}R_xCuO_2$ upon doping ($T^* = 220$ K for $x = 0.06$ and 185 K for $x = 0.08$).

At temperatures below $T_{\text{min}} = 60$ K, the resistivity shows an upturn. We note that T_{min} is independent of external magnetic fields as shown in the inset in Fig. 5(a). Figure 6 shows magnetic field dependence of the resistivity below 100 K where an upturn in resistivity is observed for $Ca_{0.94}Nd_{0.06}CuO_2$ and $Ca_{0.92}La_{0.08}CuO_2$ thin films. Negative magnetoresistance in the normal state is a common feature for both materials. Such resistivity upturns as well as negative magnetoresistances have been widely observed in high-T_c cuprate systems, but those origins have not been established [43–48]. It has also been reported that the presence of defects in the CuO_2 planes leads to a low-temperature resistivity upturn when the system is in the pseudogap state based on the Yang, Rice, and Zhang (YRZ) model [49–51]. For example, Zn substitution in the CuO_2 planes results in a nonmagnetic impurity scattering, and it is known that 2%–3% Zn substitution is sufficient to fully suppress superconductivity for $Bi_2Sr_{2-x}La_xCuO_{6+\delta}$, $La_{2-x}Sr_xCuO_4$, and $Nd_{2-x}Ce_xCuO_4$ [52–54]. For such systems, the reported electronic transport data clearly show the appearance of a resistivity upturn. In addition, the negative magnetoresistance has been observed when superconductivity is suppressed [54]. The resistivity upturns and negative magnetoresistance observed for infinite-layer $Ca_{1-x}R_xCuO_2$ films are reminiscent of the features induced by in-plane nonmagnetic impurity effects and thus we surmise that the electronic transport behaviors are simply governed by defects. Owing to the simple crystal structure of infinite-layer cuprates as illustrated in Fig. 1(a), it is very easy to violate the charge-neutrality criteria by defects. Such violation can cause severe distortions on the Cu-O bonds, ultimately leading to the breakdown of those bonds, since Ca^{2+} layers have no capability to absorb the charge imbalance caused by defects. Using the above criteria for the suppression of superconductivity by Zn doping, we estimated that the defect concentration is at least $(2 \pm 1)\%$ per CuO_2 plane for $Ca_{0.92}La_{0.08}CuO_2$ and $Ca_{0.94}Nd_{0.06}CuO_2$ thin films. The incomplete superconducting transition observed in $Ca_{1-x}Nd_xCuO_2$ is likely driven by a critical amount of in-plane defects. One may suspect that such a broad transition is attributed to the development of filamentary superconductivity [55], but this is not the case here. We confirmed that the $\rho(T)$ curves for $Ca_{0.94}Nd_{0.06}CuO_2$ film are independent of the current density (J) used for the measurements where the J was varied from 0.7 to 187 A/cm^2, which is far below the superconducting critical current density (J_c) of infinite-layer cuprates ($J_c = 5.9$ MA/cm^2) [56]. Although the in-plane defect concentration for $Ca_{0.94}Nd_{0.06}CuO_2$ and $Ca_{0.92}La_{0.08}CuO_2$ can be considered to be comparable because of identical T_{min}, no signature of superconductivity has been observed in $Ca_{0.92}La_{0.08}CuO_2$. This may be related to the appearance of the "long-c" phase as suggested for $x > 0.07$ [see Fig. 4(a)]. It is important to point out that R^{3+} substitution is unlikely the source of in-plane defects because the crystal quality is significantly improved by R^{3+} substitution.

In the YRZ model, the influences of the carrier concentrations, pseudogap, and defects have been linked to observables, e.g., Hall coefficient [57]. In Fig. 7, we plot the R_H as a function of temperature and for different doping levels. The R_H are negative from 300 to 2 K. The sign of R_H remains negative upon R^{3+} doping while the absolute value of R_H becomes smaller with increasing x, indicative of an increase in mobile carrier density upon R^{3+} doping. It is noteworthy that there are no dramatic changes in $R_H(T)$ around T^*, in contrast to other hole- and electron-doped cuprates in which abrupt changes in R_H were observed over T^* [58,59]. While it has been claimed that the observed negative R_H is evidence supporting electron-doped superconductors [60], the R_H reported for high-quality superconducting thin films of electron-doped $Sr_{0.9}La_{0.1}CuO_2$ show a change in sign as a function of temperature, and most importantly become positive at low temperatures [61,62].

Such positive R_H is expected from band structure calculation for undoped infinite-layer $CaCuO_2$ and $SrCuO_2$ as there is a large holelike Fermi surface centered at the M (π, π) point in the tetragonal Brillouin zone [63]. However, the Fermi surface mapping, reported for electron-doped infinite-layer $Sr_{1-x}La_xCuO_2$ [64], consists of $(\pi/2, \pi/2)$ holelike and $(\pi, 0)$ electronlike Fermi pockets, and is similar with what has been reported for electron-doped $R_{2-x}Ce_xCuO_4$ [65]. The discrepancy between the calculation and the experimental observations may stem from the existence of other long-range ordering phenomena. Based on the assumption that the Fermi surface topology observed for $Sr_{0.9}La_{0.1}CuO_2$ holds for electron-doped infinite-layer $Ca_{1-x}R_xCuO_2$ systems, the application of a two-band model may be suitable for interpreting our transport data. In a simple two-band model of free electrons with one hole and electron band, we derive that the Hall and diagonal conductivities of the electron band are dominant in the temperature range from 300 to 2 K, suggesting a formation of electron pockets on the Fermi surface. We suggest that electron scattering events caused by defects are reflected to the electronic transport properties observed for $Ca_{1-x}R_xCuO_2$ films. The absence of a positive R_H in $Ca_{1-x}R_xCuO_2$ may be linked to the absence of bulk superconductivity as mobile hole carriers are considered to be driving superconductivity in infinite-layer cuprate systems [61,66,67].

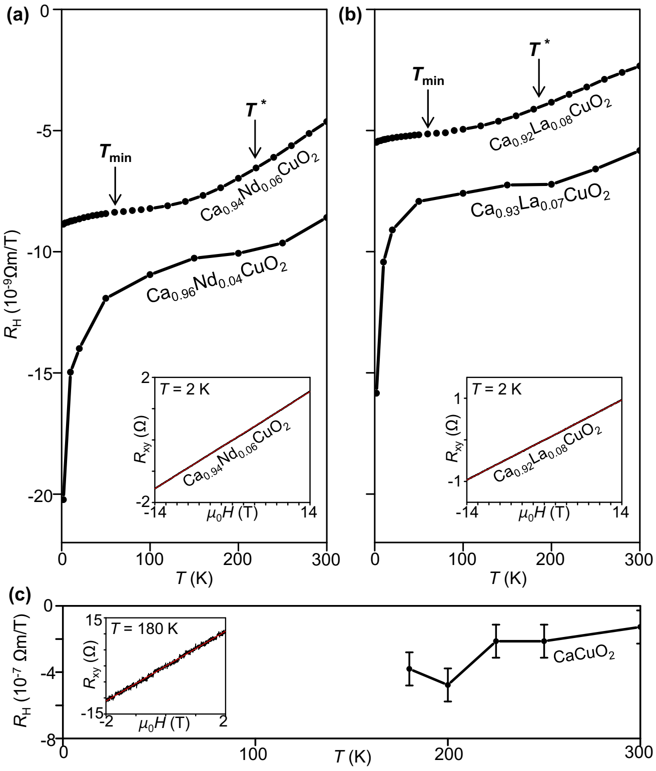

FIG. 7. Temperature dependencies of R_H for infinite-layer $Ca_{1-x}Nd_xCuO_2$ ($x = 0.04, 0.06$) (a) and $Ca_{1-x}La_xCuO_2$ ($x = 0.07, 0.08$) (b) thin films grown on (001) LSAT substrates. For comparison, R_H-T for $CaCuO_2$ is also shown (c). The insets are R_{xy}-μ_0H curves at 2 K. Black and red solid lines correspond to measurement data and linear fitted curves, respectively.

The origin of the Fermi surface reconstruction in infinite-layer cuprates is still under debate, but it has been suggested that (π, π) antiferromagnetic order coupled with electrons lets the hole band gapped [64]. On the other hand, scenarios for a formation of electron pockets have to be taken into account, e.g., charge- or spin-density waves and the pseudogap as considered for other superconducting cuprates. In infinite-layer cuprates, however, the formations of density-wave states and the pseudogap have not been reported [68]. A comprehensive understanding of our electrical transport data certainly requires further investigations.

Up to now, we focused our attention on the $Ca_{1-x}R_xCuO_2$ system with R = Nd and La. In this scenario, each Nd or La would provide one extra electron and the upper threshold for doping is determined by the solubility limit of R^{3+} in $Ca_{1-x}R_xCuO_2$. Instead of Nd or La, using Ce would provide two electrons as Ce enters the lattice in a tetravalent state. Therefore, the carrier concentration induced by Ce^{4+}

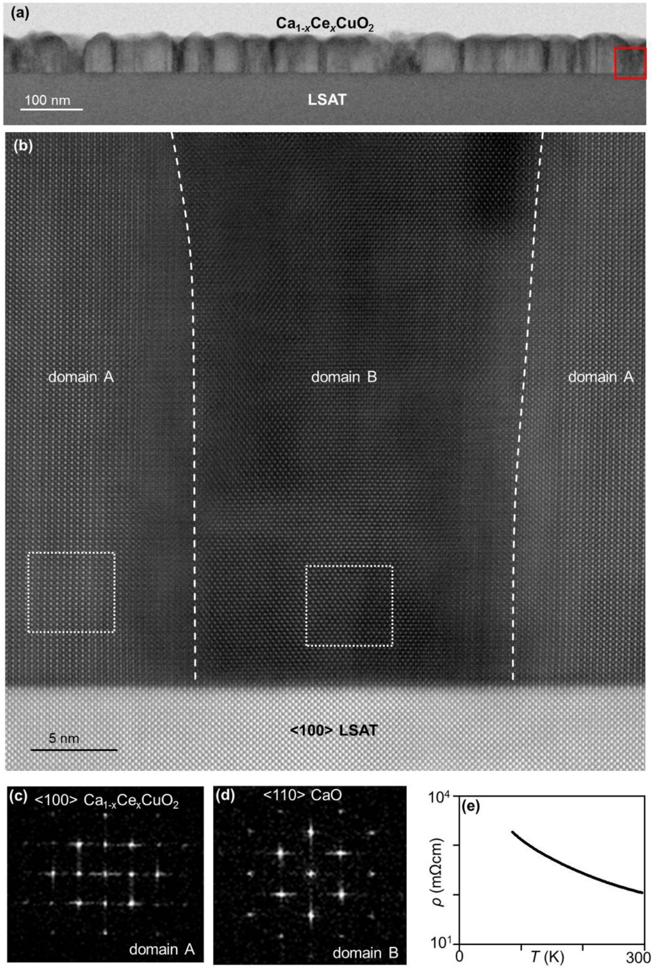

FIG. 8. Cross-sectional TEM (a) and HAADF-STEM (b) images on $Ca_{1-x}Ce_xCuO_2$ (x <0.01) thin film grown on (001)LSAT substrate. (c), (d) The fast Fourier transform patterns taken from domains A and B in (b). (e) Temperature dependence of resistivity of the $Ca_{1-x}Ce_xCuO_2$ thin film.

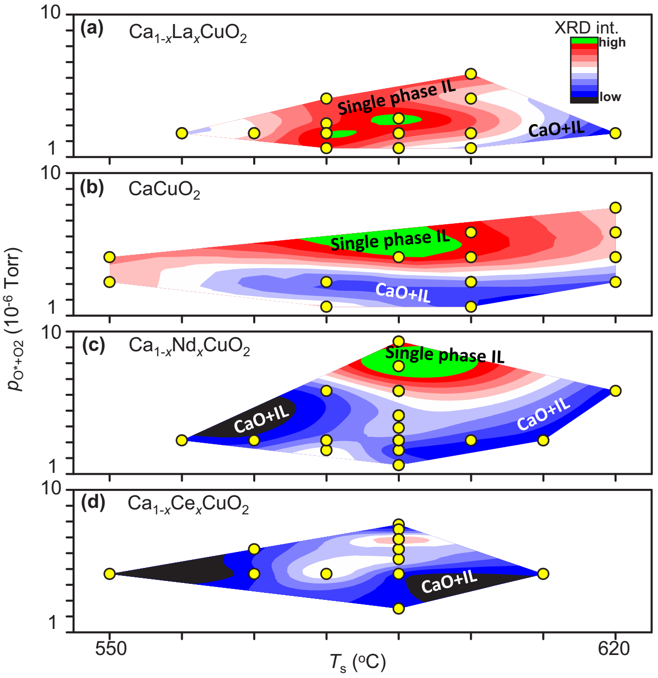

FIG. 9. (a)-(d) Counter plots of the (001) XRD peak intensities of infinite-layer $Ca_{1-x}R_xCuO_2$ ($R = La^{3+}$, Nd^{3+}, Ce^{4+}) thin films grown on (001)LSAT substrates as a function of the total pressures of atomic oxygen O* and O_2 ($p_{O^*+O_2}$) and T_s. Optimal growth conditions of $Ca_{1-x}R_xCuO_2$ where the improvements of the crystal quality and conductivity coincide, are for $Ca_{1-x}La_xCuO_2$ (a) 590 °C with rf power of 300 W and O_2 flow rate of 0.8 sccm, for $CaCuO_2$ (b) 590 °C with rf power of 300 W and O_2 flow rate of 1.5 sccm, for $Ca_{1-x}Nd_xCuO_2$ (c) 590 °C with rf of 300 W and O_2 flow rate of 2.5 sccm, and for $Ca_{1-x}Ce_xCuO_2$ (d) 590 °C with rf of 300–350 W and O_2 flow rate of 2.0 sccm. The conditions where the infinite-layer (IL) phase is stabilized are shown by red. In the blue region, impurity CaO coexists with the infinite-layer phases. (a), (b), (c), and (d) contain 36, 34, 78, and 29 different samples, respectively.

substitution is expected to be formally twice as high as by R^{3+} substitution. Figure 8(a) shows the cross-sectional TEM image of a $Ca_{1-x}Ce_xCuO_2$ film. The columnar structure of the infinite-layer phase is detected over 1 μm width. Figure 8(b) shows the high-resolution HAADF-STEM image taken at the region surrounded by square in Fig. 8(a). The atomic arrangement observed in domain A corresponds to the infinite-layer structure along the [100] direction. This is further confirmed by the fast Fourier transform (FFT) patterns taken from domain A (dotted square) [see Fig. 8(c)]. Between infinite-layer phase domains, CaO is intergrown (domain B) as shown in Figs. 8(b) and 8(d). Using EELS analysis, we confirmed that the valence states of Ce ions are tetravalent and Ca^{2+} ions are actually substituted by Ce^{4+} ions, but its substitution level is found to be below 1%. The infinite-layer phase disappears and CaO becomes dominant with increasing Ce supply during growth. For the growth of infinite-layer $CaCuO_2$ families, CaO tends to form when the oxidation conditions are weaker than what is necessary (Fig. 9). There exists a correlation that the optimum $p_{O^*+O_2}$ for the growth of $Ca_{1-x}R_xCuO_2$ increases with decreasing average ionic radius (r_i) at the Ca site [$r_i(Ce^{4+}) < r_i(Nd^{3+}) < r_i(Ca^{2+}) < r_i(La^{3+})$] [25]. For the growth of $Ca_{1-x}Ce_xCuO_2$, the oxidation power used in this work is insufficient to fully stabilize the infinite-layer phase. Defective $Ca_{1-x}Ce_xCuO_2$ thin films show insulating behavior due to disrupted CuO_2 planes [Fig. 8(e)].

The infinite-layer $CaCuO_2$ has been regarded as an exception to all superconducting cuprates because its superconductivity is still elusive. Or rather, little is known about its electronic transport properties as there exist only a few reports on the polycrystalline powder materials [16,17]. We found that single-crystalline $Ca_{0.94}Nd_{0.06}CuO_2$ thin films are at the brink of a superconducting transition below 10 K. This may arise from insufficient R^{3+} doping level such that the system remains in the underdoped regime. Optimal carrier concentrations for the induction of superconductivity are inaccessible due to the solubility limits of R^{3+} ions. The solubility limits found for $Ca_{1-x}R_xCuO_2$ are significantly lower than for electron-doped $Sr_{1-x}La_xCuO_2$ (solubility limit: $x = 0.12$). The superconductor-insulator transition has been found at $x = 0.04$–0.05 for $Sr_{1-x}La_xCuO_2$, consistent with our experiments for $Ca_{1-x}Nd_xCuO_2$. On the other hand,

$x = 0.08$ for $Ca_{1-x}La_xCuO_2$ is comparable to the optimal-doped $Sr_{1-x}La_xCuO_2$ ($x = 0.1$), but a superconducting transition has not been observed. This tangled situation indicates that the role of R^{3+} doping is not straightforward a band-filling control issue.

As shown above, R^{3+} doping significantly enhances the crystal quality of the infinite-layer phases with an increase in their Cu-O bond length ($d_{\text{Cu-O}}$). The enhanced crystal quality is plausibly related to the suppression of the microscopic defects that generate electron localization. Density-functional calculations predict that buckled or dimpled CuO_2 planes by 6° are stable in the form of infinite-layer $CaCuO_2$ [69,70]. However, buckling angles of 6° are sufficient to suppress superconductivity in $La_{2-x}Sr_xCuO_4$, $(La_{1-x}Ca_x)(Ba_{1.75-x}La_{0.25+x})Cu_3O_y$ [71,72], and this is probably true for infinite-layer cuprates as well because they cannot accommodate such large distortions in the CuO_2 planes as mentioned above. In general, the observed Cu-O bond length is associated with the strength of hybridization between Cu $3d_{x^2-y^2}$ and O $2p_{x,y}$ orbitals ($d_{\text{Cu-O}} = 1.93$ Å for $CaCuO_2$, 1.97 Å for $SrCuO_2$). This difference may be reflected by the substitution level that is required for the induction of superconductivity in infinite-layer $Ca_{1-x}R_xCuO_2$. Since the Cu-O bond length expands upon R^{3+} substitution, one can expect that higher substitution levels are necessary to induce superconductivity. This is supported by other calculations where a 50% substitution is required to fully destroy the antiferromagnetic order in $Ca_{1-x}Nd_xCuO_2$ [73]. Nonetheless, the small doping concentration commonly seen in infinite-layer $Ca_{1-x}R_xCuO_2$ [16,17] seems to be the major reason for the absence of superconductivity likely in association with defects that are insufficiently reduced by the R^{3+} substitution.

IV. CONCLUSION

In conclusion, we have grown single-crystalline electron-doped infinite-layer $Ca_{1-x}R_xCuO_2$ thin films using reactive molecular beam epitaxy. We show significant improvement on crystal quality as well as electronic conduction upon R^{3+} doping. For $Ca_{0.94}Nd_{0.06}CuO_2$, traces of superconductivity have been observed. Moreover, the temperature dependencies of resistivity suggest the formation of a pseudogap state around 200 K. At 60 K, a negative magnetoresistance is observed, most likely due to defects in the CuO_2 planes. Hall coefficient measurements suggest that the electronic conduction is driven by electronlike mobile carriers, consistent with a reconstructed Fermi surface, similar to reports for infinite-layer $Sr_{1-x}La_xCuO_2$ [64]. To achieve a positive Hall coefficient for infinite-layer $Ca_{1-x}R_xCuO_2$, the critical doping concentration (x_{cri}) is estimated to be 0.096 as shown in Fig. 10. The estimated x_{cri} is close to the optimal doping concentration for infinite-layer $Sr_{1-x}La_xCuO_2$ in which positive R_H has been reported [61].

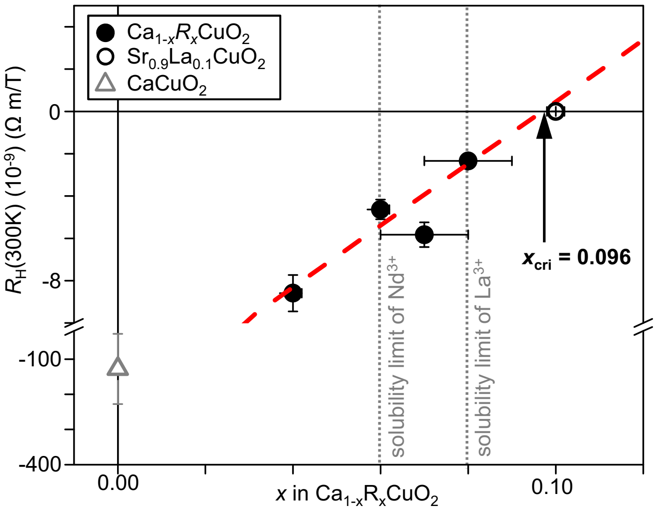

FIG. 10. R_H taken at 300 K as a function of x for infinite-layer $Ca_{1-x}R_xCuO_2$ thin films. For comparison, data for superconducting $Sr_{0.9}La_{0.1}CuO_2$ (hollow circle) [61] are also shown. The dashed red line is a linear fit to the four R_H values. For $x_{\text{cri}} = 0.096$, the R_H is expected to become positive. The solubility limits are also shown for $Ca_{1-x}Nd_xCuO_2$ and $Ca_{1-x}La_xCuO_2$ at 0.06 and 0.08, respectively.

ACKNOWLEDGMENTS

The authors gratefully acknowledge M. Naito for discussion. We thank T. Ikeda for his contribution in STEM and EELS measurements. We acknowledge H. Irie and M. Kamiya for help with Hall bar fabrication and transport measurements. We also thank Y. Taniyasu and K. Kumakura for simulating discussions.

---

[1] T. Siegrist, S. M. Zahurak, D. W. Murphy, and R. S. Roth, Nature (London) **334**, 231 (1988).
[2] M. Takano, Y. Takeda, H. Okada, M. Miyamoto, and T. Kusaka, Phys. C (Amsterdam) **159**, 375 (1989).
[3] M. Azuma, Z. Hiroi, M. Takano, Y. Bando, and Y. Takeda, Nature (London) **356**, 775 (1992).
[4] N. Kijima, H. Endo, J. Tsuchiya, A. Sumiyama, M. Mizuno, and Y. Oguri, Jpn. J. Appl. Phys. **28**, L787 (1989).
[5] T. Fujii, T. Watanabe, and A. Matsuda, J. Cryst. Growth **223**, 175 (2001).
[6] S. Karimoto and M. Naito, Appl. Phys. Lett. **84**, 2136 (2004).
[7] S. Karimoto, K. Ueda, M. Naito, and T. Imai, Phys. C (Amsterdam) **378-381**, 127 (2002).
[8] Y. Krockenberger, K. Sakuma, and H. Yamamoto, Appl. Phys. Express **5**, 043101 (2012).
[9] Y. Krockenberger, A. Ikeda, K. Kumakura, and H. Yamamoto, J. Appl. Phys. **124**, 073905 (2018).
[10] L. Maritato, A. Galdi, P. Orgiani, J. W. Harter, J. Schubert, K. M. Shen, and D. G. Schlom, J. Appl. Phys. **113**, 053911 (2013).
[11] M. Naito, S. Karimoto, and A. Tsukada, Superconduc. Sci. Technol. **15**, 1663 (2002).
[12] K. Kubo and H. Yamauchi, Phys. Rev. B **49**, 1289 (1994).
[13] K. Kubo, M. Ichikawa, N. Sugii, K. Yamamoto, and H. Yamauchi, J. Alloys Compd. **195**, 371 (1993).
[14] K. Kubo, M. Ichikawa, N. Sugii, K. Yamamoto, and H. Yamauchi, Phys. Rev. B **49**, 6919 (1994).

[15] S. Oh and J. Eckstein, Thin Solid Films **483**, 301 (2005).

[16] H. Matsuo, Y. Koike, T. Noji, N. Kobayashi, and Y. Saito, Phys. C (Amsterdam) **196**, 276 (1992).

[17] C.-J. Liu, S. Koriyama, and H. Yamauchi, Phys. C (Amsterdam) **215**, 395 (1993).

[18] H. Yamamoto, Y. Krockenberger, and M. Naito, J. Cryst. Growth **378**, 184 (2013) (the 17th International Conference on Molecular Beam Epitaxy).

[19] A. Ikeda, H. Irie, H. Yamamoto, and Y. Krockenberger, J. Mater. Res. **31**, 3522 (2016).

[20] K. Kimoto, T. Asaka, X. Yu, T. Nagai, Y. Matsui, and K. Ishizuka, Ultramicroscopy **110**, 778 (2010).

[21] S. Kobayashi, K. Inoue, T. Kato, Y. Ikuhara, and T. Yamamoto, J. Appl. Phys. **123**, 064102 (2018).

[22] S. Turner, J. Verbeeck, F. Ramezanipour, J. E. Greedan, G. Van Tendeloo, and G. A. Botton, Chem. Mater. **24**, 1904 (2012).

[23] N. Gauquelin, D. G. Hawthorn, G. A. Sawatzky, R. X. Liang, D. A. Bonn, W. N. Hardy, and G. A. Botton, Nat. Commun. **5**, 4275 (2014).

[24] N. Kobayashi, Z. Hiroi, and M. Takano, J. Solid State Chem. **132**, 274 (1997).

[25] R. D. Shannon, Acta Crystallogr., Sect. A **32**, 751 (1976).

[26] E. Wang, J.-M. Tarascon, L. H. Greene, G. W. Hull, and W. R. McKinnon, Phys. Rev. B **41**, 6582 (1990).

[27] U. Pietsch, V. Holý, and T. Baumbach, *High-Resolution X-ray Scattering*, 2nd ed. (Springer, New York, 2004), Chap. 8, p. 144.

[28] I. Groma and G. Monnet, J. Appl. Crystallogr. **35**, 589 (2002).

[29] V. M. Kaganer, O. Brandt, A. Trampert, and K. H. Ploog, Phys. Rev. B **72**, 045423 (2005).

[30] S. Bals, G. V. Tendeloo, G. Rijnders, M. Huijben, V. Leca, and D. H. A. Blank, IEEE Trans. Appl. Supercond. **13**, 2834 (2003).

[31] H. Adachi, T. Satoh, Y. Ichikawa, K. Setsune, and K. Wasa, Phys. C (Amsterdam) **196**, 14 (1992).

[32] J. Tomaschko, V. Leca, T. Selistrovski, S. Diebold, J. Jochum, R. Kleiner, and D. Koelle, Phys. Rev. B **85**, 024519 (2012).

[33] V. Leca, D. H. A. Blank, G. Rijnders, S. Bals, and G. van Tendeloo, Appl. Phys. Lett. **89**, 092504 (2006).

[34] A. Tsukamoto, J. Wen, K. Nakanishi, and K. Tanabe, Phys. C (Amsterdam) **292**, 17 (1997).

[35] S. A. Carter, B. Batlogg, R. J. Cava, J. J. Krajewski, W. F. Peck, Jr., and T. M. Rice, Phys. Rev. Lett. **77**, 1378 (1996).

[36] M. Matsuda, K. Katsumata, T. Yokoo, S. M. Shapiro, and G. Shirane, Phys. Rev. B **54**, R15626(R) (1996).

[37] M. Matsuda, K. Kakurai, J. E. Lorenzo, L. P. Regnault, A. Hiess, and G. Shirane, Phys. Rev. B **68**, 060406(R) (2003).

[38] M. Matsuda, K. M. Kojima, Y. J. Uemura, J. L. Zarestky, K. Nakajima, K. Kakurai, T. Yokoo, S. M. Shapiro, and G. Shirane, Phys. Rev. B **57**, 11467 (1998).

[39] A. Gupta, T. Shaw, M. Chern, B. Hussey, A. Guloy, and B. Scott, J. Solid State Chem. **114**, 190 (1995).

[40] D. Fuchs, P. Müller, A. Sleem, R. Schneider, D. Gerthsen, and H. v. Löhneysen, J. Appl. Phys. **112**, 103529 (2012).

[41] K. Zhao, B. Lv, L. Deng, S.-Y. Huyan, Y.-Y. Xue, and C.-W. Chu, Proc. Natl. Acad. Sci. USA **113**, 12968 (2016).

[42] S. Weyeneth, M. Bendele, F. von Rohr, P. Dluzewski, R. Puzniak, A. Krzton-Maziopa, S. Bosma, Z. Guguchia, R. Khasanov, Z. Shermadini, A. Amato, E. Pomjakushina, K. Conder, A. Schilling, and H. Keller, Phys. Rev. B **86**, 134530 (2012).

[43] T. Sekitani, M. Naito, and N. Miura, Phys. Rev. B **67**, 174503 (2003).

[44] A. Ikeda, H. Irie, H. Yamamoto, and Y. Krockenberger, Phys. Rev. B **94**, 054513 (2016).

[45] T. Sekitani, H. Sato, M. Naito, and N. Miura, Phys. C (Amsterdam) **378-381**, 195 (2002).

[46] S. Ono, S. Komiya, A. N. Lavrov, Y. Ando, F. F. Balakirev, J. B. Betts, and G. S. Boebinger, Phys. Rev. B **70**, 184527 (2004).

[47] P. Li, F. F. Balakirev, and R. L. Greene, Phys. Rev. Lett. **99**, 047003 (2007).

[48] S. Finkelman, M. Sachs, G. Droulers, N. P. Butch, J. Paglione, P. Bach, R. L. Greene, and Y. Dagan, Phys. Rev. B **82**, 094508 (2010).

[49] N. Das and N. Singh, Phys. Lett. A **380**, 490 (2016).

[50] K.-Y. Yang, T. M. Rice, and F.-C. Zhang, Phys. Rev. B **73**, 174501 (2006).

[51] T. M. Rice, K.-Y. Yang, and F. C. Zhang, Rep. Prog. Phys. **75**, 016502 (2011).

[52] J. M. Tarascon, E. Wang, S. Kivelson, B. G. Bagley, G. W. Hull, and R. Ramesh, Phys. Rev. B **42**, 218 (1990).

[53] J. Sugiyama, S. Tokuono, S. Koriyama, H. Yamauchi, and S. Tanaka, Phys. Rev. B **43**, 10489 (1991).

[54] Y. Hanaki, Y. Ando, S. Ono, and J. Takeya, Phys. Rev. B **64**, 172514 (2001).

[55] H. Xiao, T. Hu, A. P. Dioguardi, N. apRoberts-Warren, A. C. Shockley, J. Crocker, D. M. Nisson, Z. Viskadourakis, X. Tee, I. Radulov, C. C. Almasan, N. J. Curro, and C. Panagopoulos, Phys. Rev. B **85**, 024530 (2012).

[56] M. Liang, M. N. Kunchur, L. Fruchter, and Z. Z. Li, Phys. C (Amsterdam) **492**, 178 (2013).

[57] J. G. Storey, Europhys. Lett. **113**, 27003 (2016).

[58] R. Daou, N. Doiron-Leyraud, D. LeBoeuf, S. Y. Li, F. Laliberté, O. Cyr-Choinière, Y. J. Jo, L. Balicas, J.-Q. Yan, J.-S. Zhou, J. B. Goodenough, and L. Taillefer, Nat. Phys. **5**, 31 (2008).

[59] Y. Onose, Y. Taguchi, K. Ishizaka, and Y. Tokura, Phys. Rev. Lett. **87**, 217001 (2001).

[60] S. Uchida, H. Takagi, and Y. Tokura, Phys. C (Amsterdam) **162-164**, 1677 (1989).

[61] Y. Krockenberger, H. Irie, J. Yan, L. Waterston, B. Eleazer, K. Sakuma, and H. Yamamoto, Appl. Phys. Express **7**, 063101 (2014).

[62] V. Jovanovic, Z. Z. Li, F. Bouquet, L. Fruchter, and H. Raffy, J. Phys.: Conf. Ser. **150**, 052086 (2009).

[63] D. Novikov, V. Gubanov, and A. Freeman, Phys. C (Amsterdam) **210**, 301 (1993).

[64] J. W. Harter, L. Maritato, D. E. Shai, E. J. Monkman, Y. Nie, D. G. Schlom, and K. M. Shen, Phys. Rev. Lett. **109**, 267001 (2012).

[65] N. P. Breznay, I. M. Hayes, B. J. Ramshaw, R. D. McDonald, Y. Krockenberger, A. Ikeda, H. Irie, H. Yamamoto, and J. G. Analytis, Phys. Rev. B **94**, 104514 (2016).

[66] P. Fournier, P. Mohanty, E. Maiser, S. Darzens, T. Venkatesan, C. J. Lobb, G. Czjzek, R. A. Webb, and R. L. Greene, Phys. Rev. Lett. **81**, 4720 (1998).

[67] Z. Z. Wang, T. R. Chien, N. P. Ong, J. M. Tarascon, and E. Wang, Phys. Rev. B **43**, 3020 (1991).

[68] R. P. Vasquez, C. U. Jung, J. Y. Kim, M.-S. Park, H.-J. Kim, and S.-I. Lee, J. Phys.: Condens. Matter **13**, 7977 (2001).

[69] O. Jepsen, O. Andersen, I. Dasgupta, and S. Savrasov, J. Phys. Chem. Solids **59**, 1718 (1998).

[70] O. K. Andersen, S. Y. Savrasov, O. Jepsen, and A. I. Liechtenstein, J. Low Temp. Phys. **105**, 285 (1996).

[71] O. Chmaissem, J. D. Jorgensen, S. Short, A. Knizhnik, Y. Eckstein, and H. Shaked, Nature (London) **397**, 45 (1999).

[72] B. Dabrowski, Z. Wang, K. Rogacki, J. D. Jorgensen, R. L. Hitterman, J. L. Wagner, B. A. Hunter, P. G. Radaelli, and D. G. Hinks, Phys. Rev. Lett. **76**, 1348 (1996).

[73] P. De La Mora and G. Tavizón, Int. J. Quantum Chem. **80**, 499 (2000).